Microvoid Formation during Shear Deformation of Ultrahigh Strength Steels

J.G. COWIE, M. AZRIN, and G.B. OLSON

Shear tests were performed on ultrahigh strength steels under both quasistatic and dynamic conditions, aimed at elucidating the fundamental mechanisms of shear localization underlying both adiabatic shear localization and fracture processes. Experiments were also devised to study the effect of hydrostatic pressure and austenitizing temperature on the critical strain to localization. Experimental evidence strongly suggests that strain localization in the steels investigated is driven by microvoid softening controlled by nucleation at 100 nm scale particles. This is supported by the observed pressure dependence of the instability strain, enhanced resistance to shear instability with particle dissolution, and direct observation of microvoids at these particles in deformed material. For the steels investigated with approximately equivalent strength levels, a direct correlation between the crack extension force and shear instability is demonstrated. Consequently, both fracture toughness and shear localization are dependent on the size, type, and distribution of second phase particles.

I. INTRODUCTION

THE phenomenon of plastic shear instability and flow localization is of considerable interest due to its important role in fracture processes in many high strength steels, especially in the ultrahigh-strength (UHS) range. It is also of special concern in Army applications of these steels because of its role as a principal failure mode in ballistic penetration. The latter case has been traditionally modeled as a continuum plastic instability arising from the thermal softening associated with deformation under adiabatic conditions. Models based on isothermally derived empirical constitutive relations have been used to account for strain localization conditions observed in high strain rate shear tests, but recent experiments have cast doubt on the validity of this approach.[1] Here we report further results of shear tests conducted under both quasistatic and dynamic conditions, aimed at elucidating the fundamental mechanisms of shear localization underlying both fracture and ballistic penetration processes.

II. BACKGROUND

The phenomenon of deformation localization as it occurs in ballistic penetration is illustrated in Figure 1,[2] showing the localized deformation mode of failure, commonly referred to as adiabatic shear. The plastic flow after the onset of shear instability is concentrated in thin shear bands which appear white after metallographic etching. The through-thickness localized flow produces a "shear plugging" failure mode in which the material ahead of the projectile is ejected as a solid piece absorbing relatively little associated energy.

Much has been written over the past 40 years on the subject of shear localization. In a recent review, Cowie and Tuler[3] describe the various modeling approaches: flow softening, deformation heating, textural softening, and void nucleation softening. The review also describes the relationship between shear instability and fracture toughness. The reviews of Rogers[4,5] and Bedford *et al.*[6] give an excellent overview of the general phenomenon including the microstructures resulting from localized flow. The continuum plasticity theory of adiabatic flow localization is treated by Clifton,[7] and a general survey of strain localization is given by Argon.[8] A concise treatment of the specific role of adiabatic shear in armaments and ballistics can be found in the review of Samuels and Lamborn.[9] Olson *et al.*[10] endeavored to computer model the ballistic penetration of high strength steel using experimentally derived constitutive flow relations, but met with limited success. The authors proposed that the material exhibited a pressure dependence that the conventional thermal softening models could not describe. Experiments were designed to determine how the pressure dependence affects the deformation of UHS steels. More recent research by Azrin *et al.*[1] showed that the critical strain for shear localization in high strength 4340 steel is nearly identical for both isothermal (quasistatic) and adiabatic (dynamic) loading conditions. While thermal softening undoubtedly provides a contribution to the measured stress-strain relations, this result of nearly identical instability strains and shear localization behavior in UHS steels at both high and low strain rates indicated that another flow softening phenomenon was equally important. As was reviewed in Reference 10, observations that the instability strain is strongly influenced by the hydrostatic component of stress, together with metallographic evidence of microvoid nucleation, indicate that fracture related processes can also contribute to the strain softening effects underlying plastic shear localization.[11,12,13] Such phenomena must also be taken into account for a complete understanding of shear localization and shear banding.

The present study was initiated to obtain experimental evidence of microvoid nucleation preceding localized deformation during simple shear of UHS steels. Experiments were also devised to study both the effect of

J.G. COWIE, Materials Research Engineer, and M. AZRIN, Supervisory Metallurgist, are with the U.S. Army Materials Technology Laboratory, Watertown, MA 02172-0001. G.B. OLSON is Professor at Northwestern University, Evanston, IL 60208.

Manuscript submitted March 28, 1988.

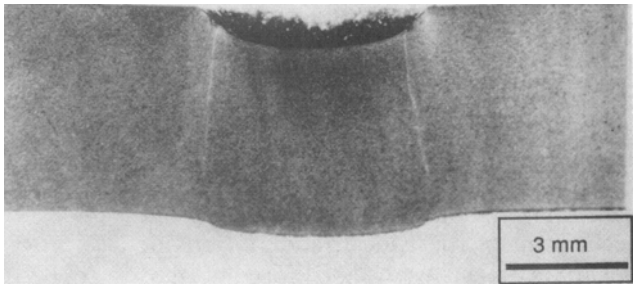

Fig. 1—Photomicrograph of a 4340 steel Rc 52 plate (5.6 mm thick) that underwent a localized deformation mode of failure during ballistic impact. Note the white etched shear bands beneath the area of impact.

hydrostatic pressure and austenitizing temperature on the critical strain to localization. Two different simple shear specimen geometries were compared. Because of its influence on fracture related processes of potential importance to shear instability, the role of melt practice was also examined. Stress-strain data and corresponding strain profiles were obtained from each test in order to quantify the flow behavior in addition to accurately determining the instability strain.

III. MATERIALS AND METHODS

Two specimen geometries, thin wall torsion and double linear shear configurations, were tested under both adiabatic and isothermal conditions. Dynamic torsion tests were performed on a torsional impact apparatus incorporating a flywheel. Torque to the specimen is applied by a steel bar pneumatically engaged to lugs on the rotating flywheel. Flywheel rotational frequency is monitored by a velocimeter, while applied torque is measured by a strain gage load cell adjacent to the specimen. Wooden dowels were inserted into the specimen to minimize buckling. These dynamic tests were performed at an imposed strain rate of 10^2 per second to ensure essentially adiabatic deformation conditions in the specimens. Isothermal torsion tests were run on an MTS servo-hydraulic test machine at a strain rate of 10^{-3} per second. Results from the thin wall torsion experiments were reported previously.[1]

Double linear shear specimens were also tested under both quasistatic and dynamic conditions. These specimens are machined from standard sized Charpy blanks. They have two narrow gage sections which are displaced simultaneously in simple shear (Figure 2). Dynamic tests were performed in a modified instrumented Charpy impact machine. The Charpy specimen fixture was replaced with one that rigidly holds the ends of the double linear shear specimen. In addition, the pendulum weight was increased by 60 pct. The shear fixture may also apply up to 2250 N normal compressive load to the specimen's end while the specimen is being sheared. The load-time curve generated by the strain gage instrumented tup is recorded and stored in the memory of a Nicolet high speed digital oscilloscope. These dynamic tests were performed at an imposed strain rate in excess of 10^4 per second. Quasistatic double linear shear tests were run on a Tinius Olsen hydraulic tension/compression test machine at a strain rate of 10^{-3} per second.

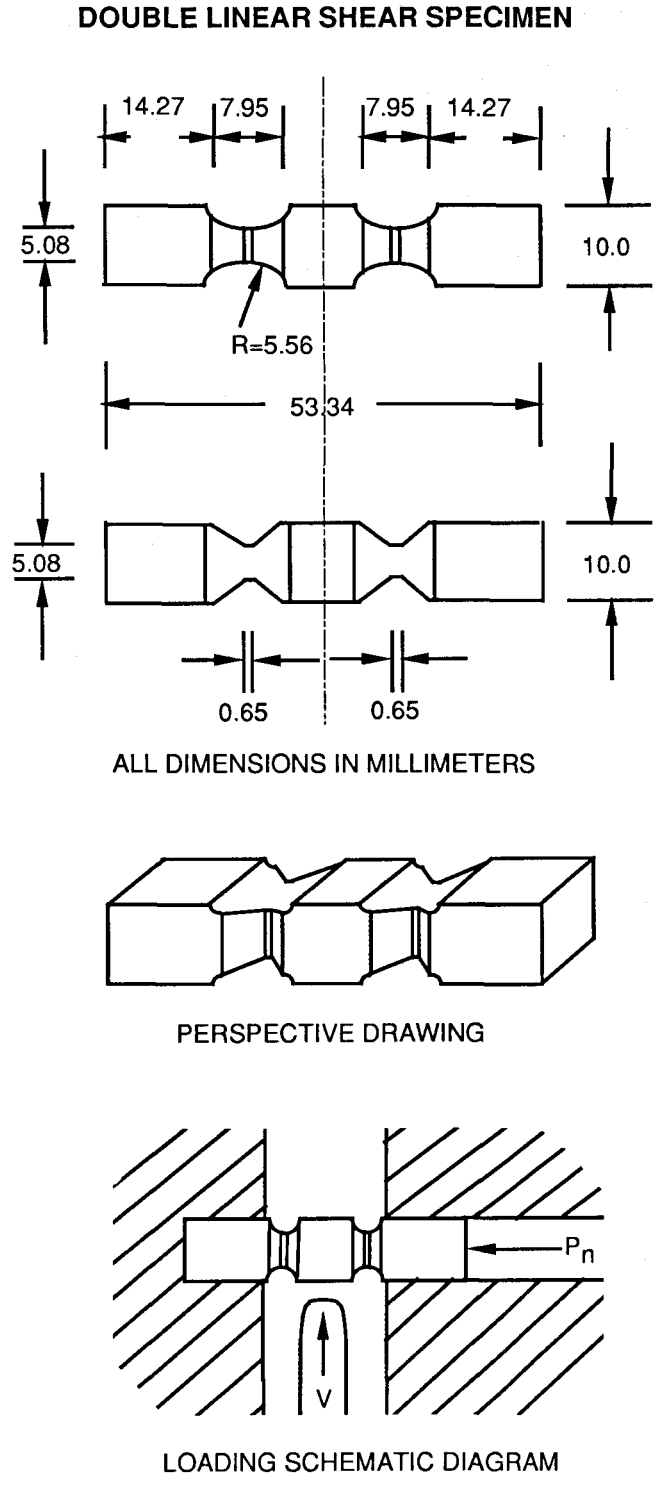

Fig. 2—Mechanical drawing, perspective drawing, and loading schematic diagram of a double linear shear specimen. The specimen is sheared within the two reduced sections at a preselected speed (V) while an axial load (P_n) can be superimposed on one end.

Typical shear stress-shear strain curves generated from these tests are presented in Figures 3 and 4. These represent a rare earth modified (REM) 4130 steel (composition presented in Table I), austenitized at 840 °C and tempered 1 hour at 535 °C and 200 °C to give hardnesses of Rc 33 and 48, respectively.

To determine precise strain profiles, four longitudinal

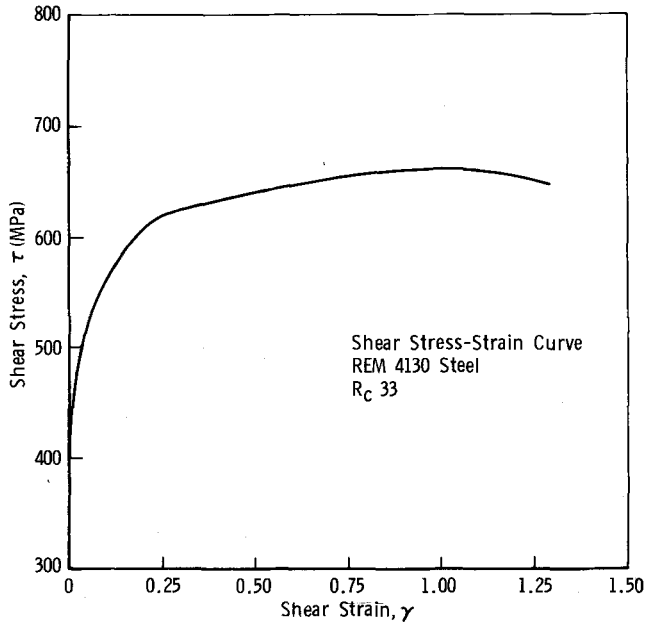

Fig. 3—Plastic shear stress-strain curve obtained from a quasistatic linear shear test of REM 4130 steel at Rc 33 (535 °C temper). Shear strain at maximum stress is 110 pct.

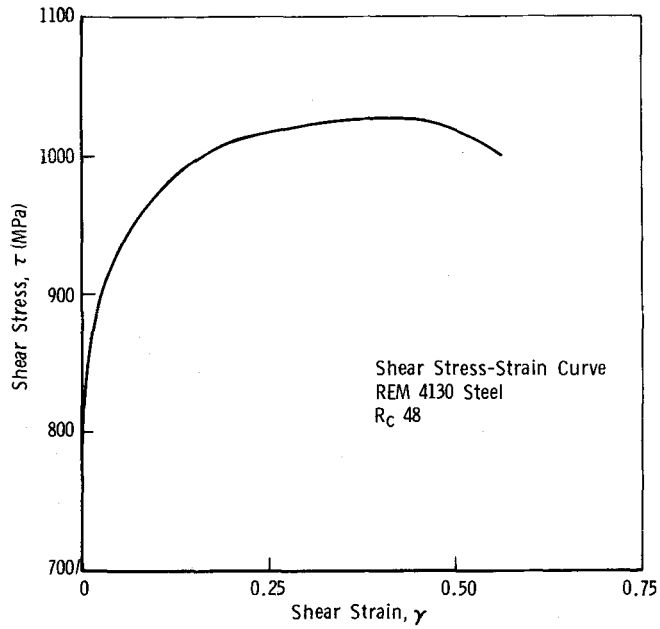

Fig. 4—Plastic shear stress-strain curve obtained from a quasistatic linear shear test of REM 4130 steel at Rc 48 (200 °C temper). Shear strain at maximum stress is 45 pct.

scribe marks were drawn onto the gage section of each specimen before testing. After testing, shear strain as a function of the position along the specimen axis was determined from the local angle of the scribe marks relative to the specimen centerline as measured in a Leitz universal measuring microscope. Dynamic tests were run to failure, while quasistatic tests were generally run until sufficient flow localization to produce a load drop of approximately 10 pct.

Typical strain profiles obtained from isothermal tests are presented in Figures 5 and 6 which correspond to the stress-strain curves in Figures 3 and 4, respectively. Intense strain localization is found adjacent to the gage section walls. This is consistent with both a computer simulation of simple shear of a rectangular body[10] and a finite element stress analysis of the double linear shear specimen geometry and loading by Tracey and Perrone.[14] Note that the shear strain plateaus (henceforth defined as the macroscopic instability strain) on the strain profiles correspond with the shear strains at peak stress on their corresponding stress-strain curves. Comparison of the instability strain data for both torsion and linear-shear test specimen geometries (Figures 7 and 8) confirms that the two configurations give nearly identical results.

IV. RESULTS

A. *Effect of Melting Practice*

Because of its influence on fracture related processes of potential importance to shear localization, the role of melt practice was also examined. Three commercial heats of 4340 steel processed by air melt (AM), electroslag remelt (ESR), and vacuum arc remelt (VAR) practices were evaluated (compositions presented in Table II). The shear specimens were machined from heat-treated blanks austenitized at 840 °C and tempered 1 hour at 650 °C, 535 °C, 335 °C, and 160 °C to give hardness levels of Rc 30, 40, 48, and 56, respectively. Dynamic and quasistatic tests revealed no significant effect of melting practice, with one exception. Under isothermal conditions, the air-melted material tempered at 535 °C (Stage III temper) proved consistently to have a higher instability strain than its VAR and ESR counterparts. Structurally, the only observable difference was the slightly smaller prior austenite grain size for the AM material. The structure of the 4340 steel given this tempering treatment contains intra-lath cementite. It is possible that the shear localization resistance is influenced by the length of void-nucleating cementite particles which, in turn, scale with the martensite packet and prior austenite grain sizes.

B. *Effect of Strain Rate*

Plotting all the instability strain data for both adiabatic (Figure 7) and isothermal (Figure 8) test conditions together (Figure 9), we observe little effect of strain rate on the instability strain, particularly at the higher strength levels. The linear shear tests spanned seven orders of magnitude in strain rate from isothermal to adiabatic test conditions. The resulting instability strains for the highest strength material (Rc 56) were nearly identical

Table I. Rare Earth Modified 4130 Steel Composition (Wt Pct)

C	Mn	P	S	Si	Cr	Mo	Ti	B	Ce
0.30	0.62	0.004	0.008	0.29	1.05	0.20	0.051	0.002	<0.005

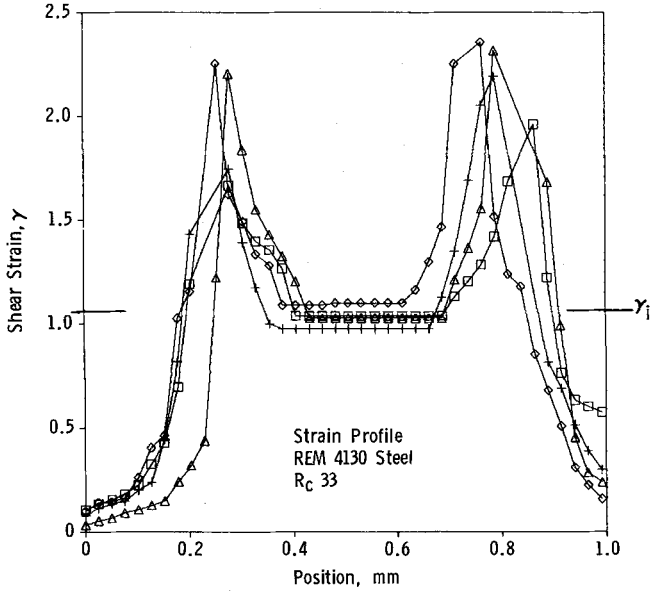

Fig. 5—Strain profiles obtained from a quasistatic linear shear test of REM 4130 steel at Rc 33 (535 °C temper). The mean plateau strain, defined as the macroscopic instability strain, is 110 pct.

(Figures 9 and 10). The flow stress increased nearly 50 pct from quasistatic to dynamic test conditions.

The results of these tests imply that there is little effect of thermal softening (absent in the isothermal tests) on the instability strain at high strength levels. This implies a dominant role of a microstructural instability in the shear localization behavior under pure shear conditions.

C. *Effect of Pressure*

In order to test whether UHS steels exhibit the pressure dependent behavior previously observed in lower strength steels,[10] double linear shear tests were run quasistatically with a superimposed axial compressive load.

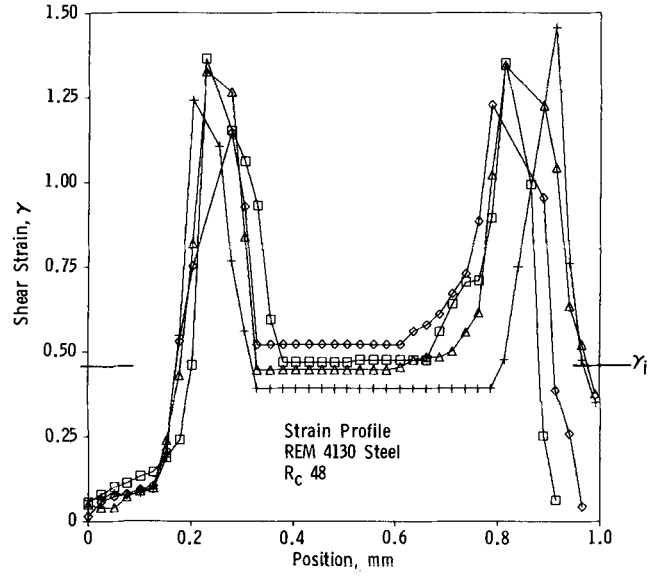

Fig. 6—Strain profiles obtained from a quasistatic linear shear test of REM 4130 steel at Rc 48 (200 °C temper). The mean plateau strain, defined as the macroscopic instability strain, is 45 pct.

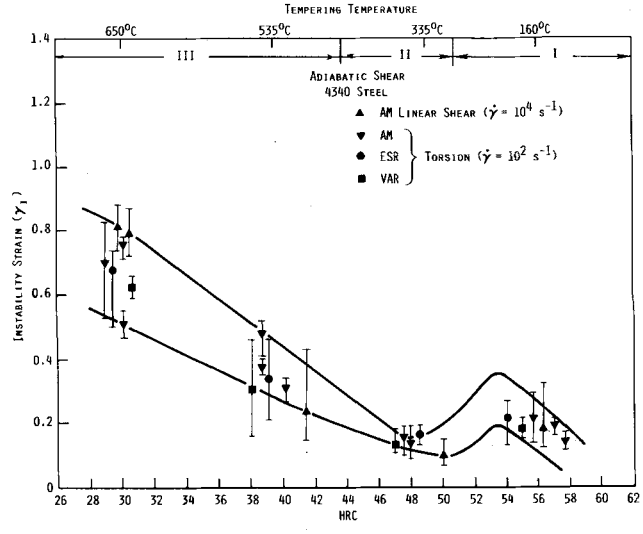

Fig. 7—Comparison of instability strains measured in dynamic torsion and linear shear tests of AM, ESR, and VAR 4340 steel.

Finite element calculations indicate that the stress component arising from this axial load reasonably approximates uniaxial stress once plastic shearing is underway. Axial compressive stresses of 1/6 and 1/3 the material's tensile yield stress were used. The stress-strain results quite clearly show pressure dependent behavior (Figures 10 and 11). As the axial stress is increased from 0 to 1/3 of the yield stress, the instability strain is increased quite substantially for all four hardness levels investigated.

The microstructure of the highest strength (Stage I tempered) material consists of a martensitic lath matrix with a fine epsilon carbide dispersion. In addition, there are submicron sized second phase particles which act as grain refiners (Figure 12). These second phases (undissolved during austenitizing) have been identified by Gore[15] to be primarily alloy (Fe,Cr,Mo) carbides of the type $M_{23}C_6$ with a mean diameter of 171 nm and a vol fraction of 0.44 pct when austenitized at 870 °C. The carbides, with an interparticle mean free path of 670 nm,

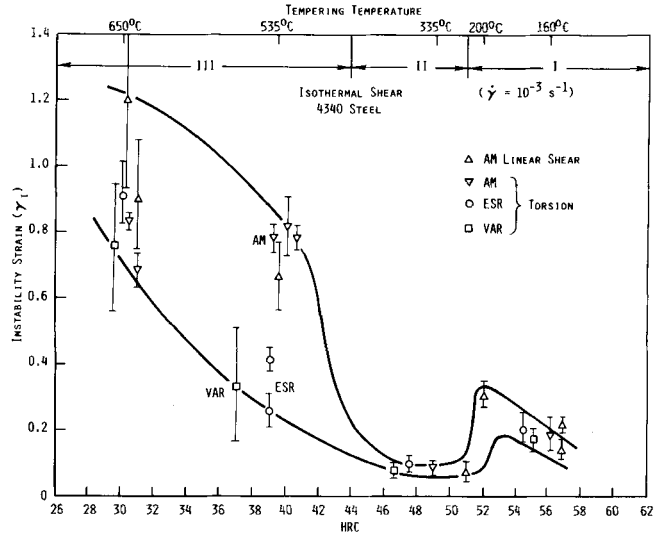

Fig. 8—Comparison of instability strains measured in quasistatic torsion and linear shear tests of AM, ESR, and VAR 4340 steel.

Table II. 4340 Steel Compositions (Wt Pct)

Melting Practice	C	Mn	P	S	Si	Cr	Ni	Mo	Cu
AM	0.41	0.75	0.005	0.011	0.25	0.79	1.71	0.24	0.13
ESR	0.41	0.70	0.008	0.001	0.26	0.90	1.73	0.22	0.21
VAR	0.42	0.46	0.009	0.001	0.28	0.89	1.74	0.21	0.19

are expected to interact during plastic deformation,[16] leading to cooperative microvoid nucleation. Interactions between dispersoids occur when the plastic zones of the neighboring particles touch.[16,17] The critical stress for nucleation has been found to be dependent on the interparticle spacing to particle radius ratio.[17] Large or closely spaced dispersoids nucleate voids at relatively small strains, and ultimately degrade the material's ductility.[18] Figure 13 presents a TEM photomicrograph of sheared material showing a pair of carbides linked by microvoids. The photograph has been deliberately overdeveloped to clearly show the voids, and a schematic representation is also shown for clarity. This thin foil specimen was removed from the gage section of a linear shear specimen which was strained to instability. The micrograph was taken in the region which received only uniform deformation and had stopped straining once instability occurred. It was observed that many carbides exhibited this type of behavior. The directions of void growth appear aligned in the direction of the principal stress. Shear cracks linked pairs of carbides predominantly along the direction of the imposed shear direction, 45 deg to the principal stress direction. These experimental observations are consistent with the finite element investigation of interacting void pairs by Tracey and Perrone.[16] Although specimen preparation by electropolishing may have enlarged the voids, no such voids were observed in identically prepared foils taken from the undeformed grip ends of the specimens. We thus conclude that the voids are genuinely produced by the plastic deformation.

Summarizing, the pressure dependent behavior of the instability strain can be attributed to the stress required to debond the second phase particles from the matrix and to form microvoids. This interpretation is supported by the recent analysis by Hutchinson and Tvergaard[19] on microvoid nucleation softening as a basis for shear instability.

D. *Effect of Austenitizing Temperature*

A further test of the role of second phase particles in shear localization can be made by raising the austenitizing temperature to dissolve alloy carbides. Gore[15] has demonstrated that raising the austenitizing temperature from 870 °C to 1200 °C in the same VAR 4340 steel examined here fully dissolves the Cr-Mo alloy carbides, leaving primarily fine 80 nm Ti (C,N) particles at a much reduced vol fraction of 0.05 pct. Such a change in the amount and character of undissolved second-phase particles can be expected to alter significantly the critical strain for microvoid nucleation softening. This should be most pronounced in Stage I tempered material where the ultrafine epsilon carbides precipitated during tempering should not contribute to microvoid nucleation, and the role of the undissolved particles would thus be greatest. Although the size, type, and distribution of the fine dispersoids found in VAR 4340 and AM 4340 are not identical, the tendency for their dispersoids to dissolve into the matrix is the same. Therefore, a

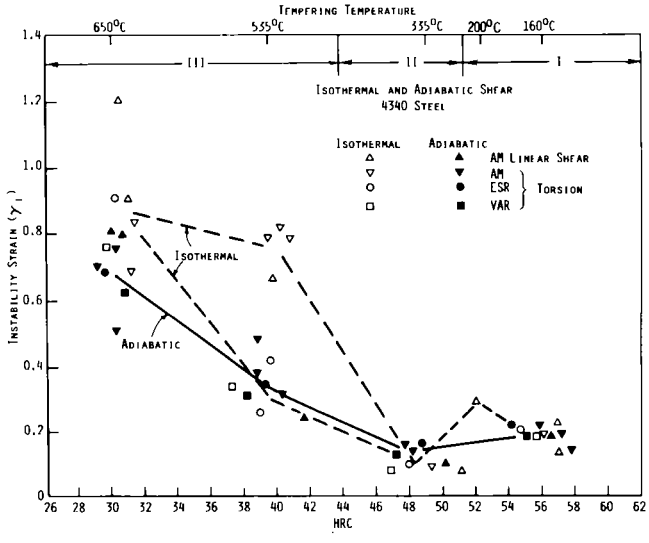

Fig. 9—Comparison of instability strains measured in both dynamic and quasistatic shear tests of AM, ESR, and VAR 4340 steel.

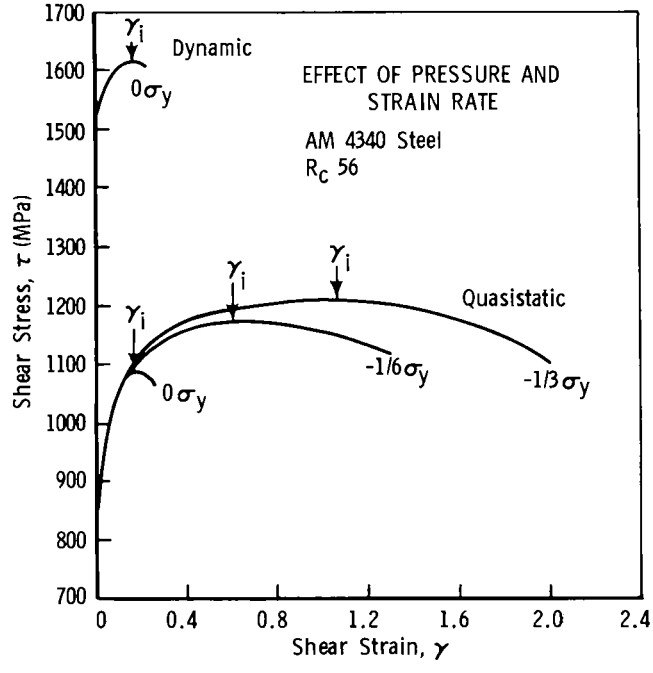

Fig. 10—Plastic shear stress-strain curves obtained from both dynamic and quasistatic linear shear tests of an AM 4340 steel at Rc 56, with three different imposed axial compressive stresses: 0, 1/6, and 1/3 the yield strength.

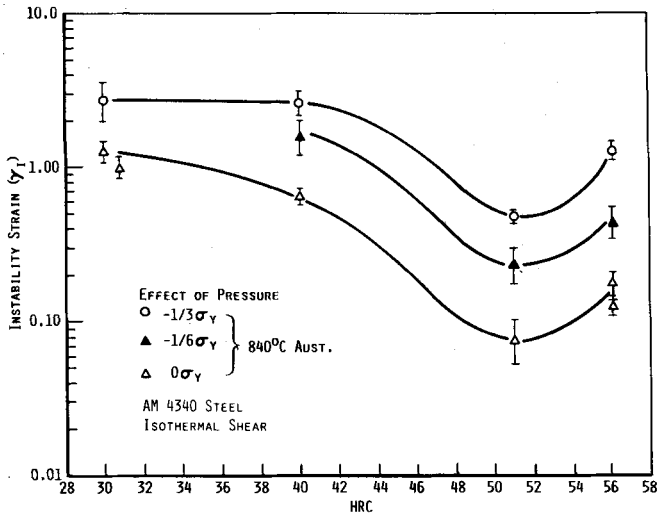

Fig. 11—Comparison of instability strains of an AM 4340 steel with three different imposed axial compressive stresses: 0, 1/6, and 1/3 the tensile yield strength.

comparison of the shear instability of AM 4340 to the dissolution of the fine particles in VAR follows.

A comparison of the shear instability strains measured in linear shear tests on the AM 4340 austenitized at 840 °C (as in Figure 8) and 1100 °C is presented in Figure 14

Fig. 12—TEM micrograph of the microstructure of 4340 steel at Rc 55, which consisted of undissolved alloy carbides in a matrix of heavily dislocated lath martensite.

using the same four tempering conditions as in Figure 8. Material well tempered in Stage III to Rc 30 shows no significant increase in instability strain, consistent with a dominant role of the 100 nm cementite particles precipitated during tempering. For lower tempering temperatures (high hardness), where the carbides precipitated on tempering are finer, there is a pronounced increase in instability strain with 1100 °C austenitizing, suggestive of an important role of the undissolved alloy carbides in shear localization.

The pressure sensitivity of the shear instability strain in the 1100 °C austenitized material is represented in Figure 15 comparing the behavior without and with a normal compressive stress of 1/6 the yield stress. Though the controlling particles may be changed by austenitizing conditions, the persistent pressure sensitivity implies that microvoid softening continues to be the dominant strain softening mechanism. As depicted in Figure 14, the AM 4340 tempered in Stage I at 160 °C to Rc 56 hardness shows an increase in the instability strain from the 0.12 to 0.18 range to 0.23 when the austenitizing temperature is raised from 840 °C to 1100 °C. This is not as large an increase as observed for the Stage II and early Stage III temper conditions (Rc 50 and 40, respectively). A further investigation by Gore[15] of the effect of austenitizing temperature in the range of 870 to 1200 °C on the instability strain in the VAR 4340 tempered in Stage I at 200 °C to Rc 52 has shown a slight monotonic decrease with increasing austenitizing temperature. The effect has been attributed to a contribution of crystal-plasticity-based strain softening mechanisms which may be promoted by grain coarsening. As mentioned previously in discussion of melt practice comparison in Figure 8, the AM 4340 shows greater grain coarsening resistance than the cleaner VAR 4340 and such grain coarsening effects may not have had as strong an influence in the 840 to 1100 °C comparison for the AM material. Pressure sensitivity of the very coarse-grained material has not yet been evaluated to test for a change in strain softening mechanism.

The observed increase in the instability strain with particle dissolution in the AM 4340 lends further support for the role of microvoid nucleation softening in shear localization in conventionally treated material. However, the indication that severe grain coarsening can introduce other strain softening contributions limits the practical utility of high temperature austenitizing treatments for enhancement of mechanical properties.

E. *Role of Tempering Stage*

While our studies have focused primarily on the behavior of 4340 steel, the rare-earth modified (REM) 4130 steel represented in Figures 3 to 6 was included to extend the hardness range that could be examined in each stage of tempering. Figure 16 summarizes the combined linear-shear test results of the AM 4340 and REM 4130 steels in a linear plot of instability strain *vs* Rc hardness. Grouping the data for the three tempering stages, Stage I tempering appears to show a superior combination of shear instability resistance and hardness (strength). This can be attributed to the fine scale of the epsilon carbides precipitated on tempering, which should not act as

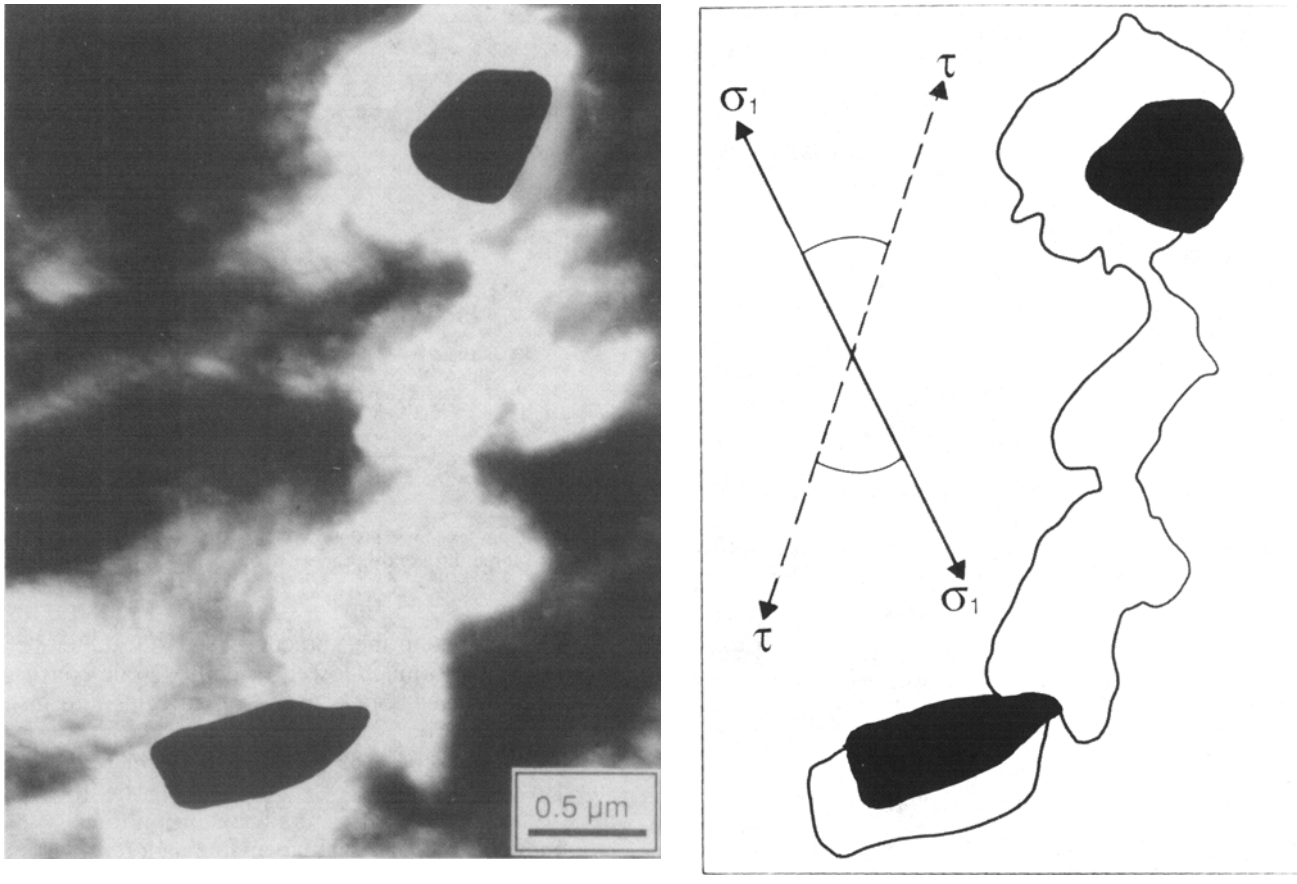

Fig. 13—TEM micrograph of microvoid nucleation around a pair of undissolved alloy carbides. The accompanying schematic illustrates the direction of shear and principal stress.

microvoid nucleation sites. For Stage III tempering, strength is provided by precipitated cementite which is sufficiently coarse to participate directly in earlier microvoid nucleation at a given hardness level. The general downward trend of instability strain with hardness for each class of microstructure is presumably associated with reaching critical interface stresses at lower strains when the matrix flow stress is increased.

The much lower shear instability resistance of the Stage II tempered microstructure correlates with a minimum in the Charpy impact energy commonly known as the tempered martensite embrittlement trough. This implies a connection between low Charpy energy and early shear localization. As the instability strain is still pressure sensitive in this stage (Figure 11), the embrittlement

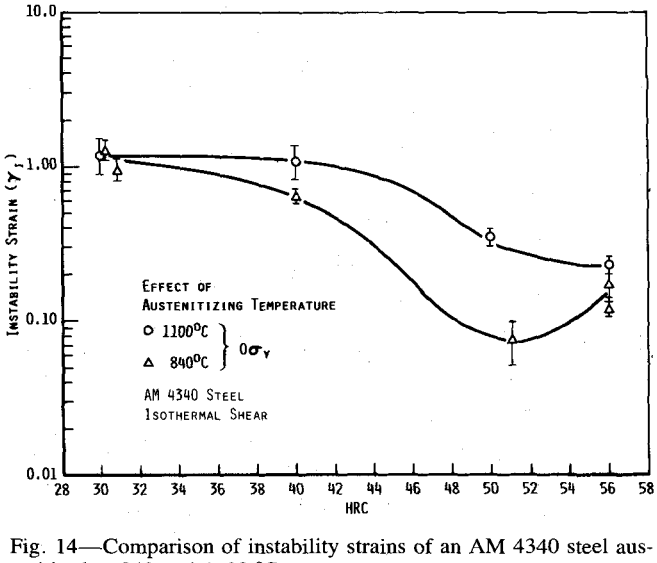

Fig. 14—Comparison of instability strains of an AM 4340 steel austenitized at 840 and 1100 °C.

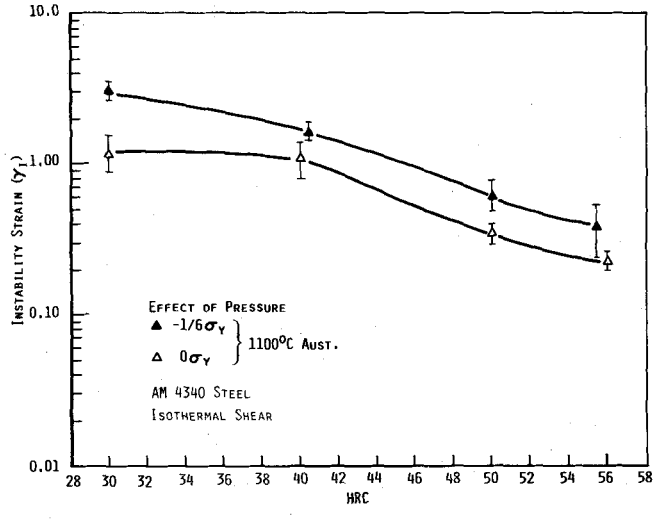

Fig. 15—Comparison of instability strains of an AM 4340 steel austenitized at 1100 °C with different imposed axial compressive stresses: 0 and 1/6 the yield strength.

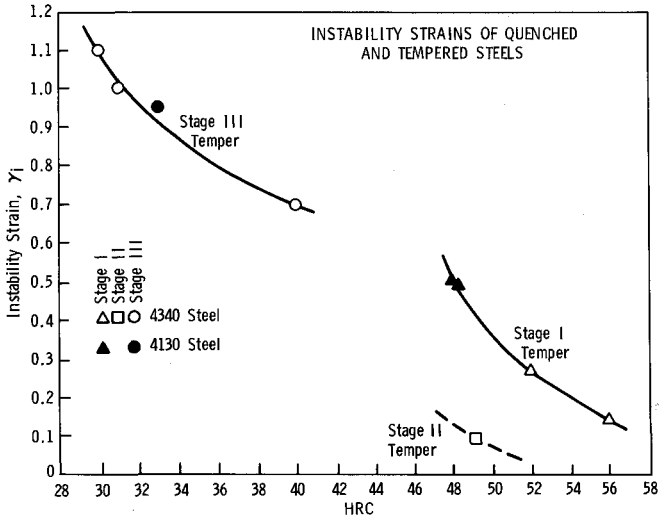

Fig. 16—Comparison of instability strain curves of quenched and tempered steels having Stage I, Stage II, and Stage III structures.

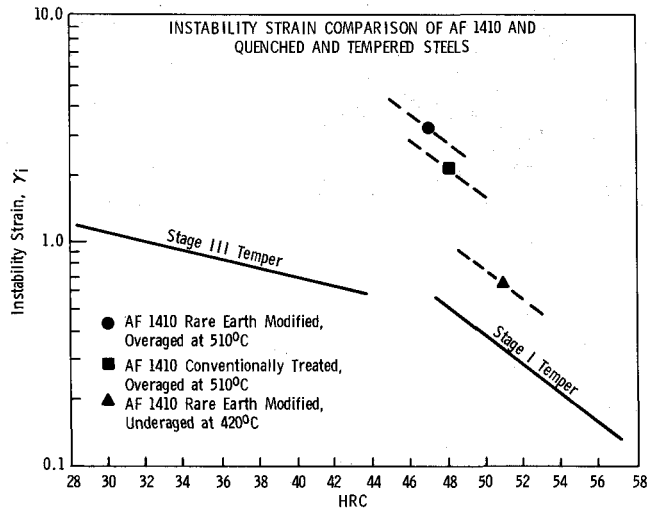

Fig. 17—Comparison of instability strains of quenched and tempered steels and three differently processed AF 1410 steels.

phenomena associated with retained austenite decomposition in Stage II presumably cause earlier microvoid nucleation.

F. *Comparison with Secondary Hardening Steel: Toughness Correlations*

Secondary hardening AF1410 steel achieves high strength from the precipitation of fine M_2C carbides during tempering at 510 °C. Optimum strength/toughness combinations are achieved in a 5-hour temper "overaged" condition for which completion of M_2C precipitation causes dissolution of coarser cementite particles which precipitate earlier during tempering. Optimum melt practice generally involves rare-earth treatments for gettering of sulfur. The shear instability resistance in the standard 510 °C/5 hours tempered condition was measured for two heats with and without the rare earth treatment (compositions presented in Table III). Also examined was rare-earth treated material tempered 5 hours at 420 °C to provide an "underaged" material of comparable hardness but with the cementite particles present.

The results are compared with those of the Stage I and Stage II tempered 4340 and 4130 steels in a semi-log plot *vs* hardness in Figure 17. For the standard 510 °C/5 hours temper, the AF1410 shows substantially higher shear instability resistance compared to the Stage I tempered steels. The material without rare-earth treatment is shown to contain relatively fine chromium sulfides. Replacement by rare-earth sulfides and oxysulfides in the rare-earth treated material evidently enhances shear instability resistance, in contrast to the 4340 steels' relative insensitivity to melt practice. The 420 °C tempered material shows a much lower instability strain consistent with the expected role of undissolved cementite in microvoid nucleation.

Fracture toughness of the same three materials measured at Carpenter Steel[20] shows a similar trend *vs* hardness. Expressed as critical crack extension force G_{Ic}, the toughness is compared with available data for 4340 steel in Figure 18. A test of the apparent G_{Ic}-instability correlation is plotted in Figure 19, including data for the VAR 4340 austenitized at 840 °C and tempered 2 hours at 200 °C to a comparable hardness level of Rc 50. The good correlation observed is in line with the proposed roles of second-phase particles in shear localization and ductile fractures.[19,20]

Further support for the important role of microvoid nucleating particles in the ductile fracture behavior of AF1410 is provided by the solution treatment study of Schmidt and Hemphill.[20] A significant toughness enhancement is obtained on raising the solution treatment temperature from 830 °C to 885 °C. After conventional treatment at 830 °C, the microstructure contains chromium-rich $M_{23}C_6$ carbides of 900 to 1800 nm diameter along with smaller 40 to 80 nm molybdenum-rich MC carbides. After 885 °C solution treatment, the $M_{23}C_6$ carbides are fully dissolved, leaving only the finer MC particles.

G. *Microvoid Observations*

The fine 100 nm scale of microvoid formation makes microscopy observations difficult compared to the more

Table III. AF1410 Steel Compositions* (Wt Pct)

Alloy	C	Mn	P	S	Si	Cr	Ni	Mo	Co	Ti	Al	N**	O**	Ce
Conventional	0.176	<0.01	0.002	0.003	<0.01	2.08	10.3	1.06	14.3	<0.01	0.003	10	8 to 11	<0.001
REM	0.167	0.02	0.003	0.002	0.01	2.08	10.2	1.05	14.3	0.013	0.004	<10	18	<0.005

*Courtesy of Carpenter Technology Corporation.
**Parts per million.

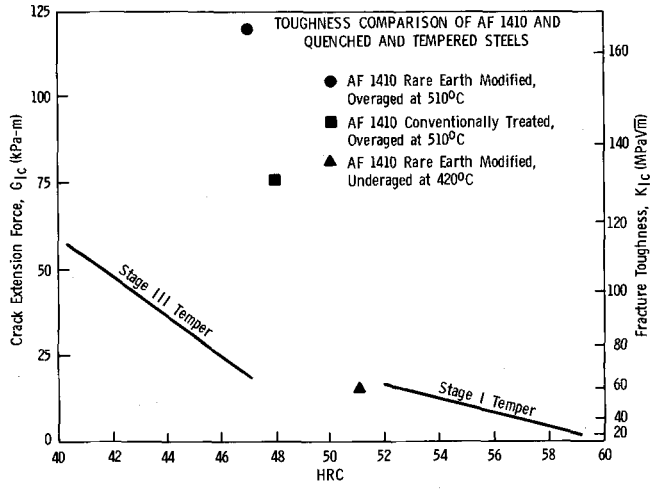

Fig. 18—Toughness comparison of AF1410 and quenched and tempered steels.

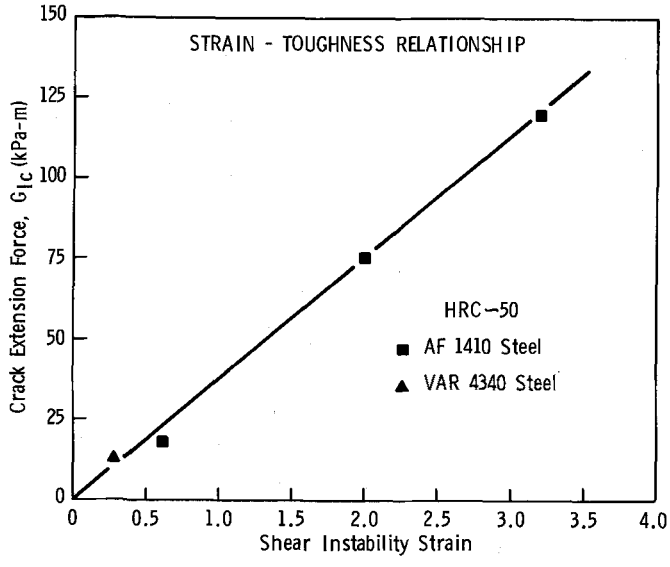

Fig. 19—Instability strain-fracture toughness relationship measured on three AF1410 steels and one VAR 4340 steel.

familiar problem of >100 nm scale "primary" void formation, which has been well studied by light metallography. An effort is underway to find further direct evidence for microvoid formation beyond the thin-foil TEM observations of Figure 13, using SEM metallography of lightly etched polished surfaces taken from the gage sections of interrupted shear tests. Referring to the shear stress-strain curve for Rc 55 VAR 4340 in Figure 20, specimens have been examined for the strained conditions denoted by:

(A) before maximum stress
(B) at maximum (instability) stress
(C) after maximum stress
(D) near fracture.

The shear strain profiles taken from these four specimens are presented in Figure 21, showing the progressive development of a strain plateau at the instability strain and the growth of strain peaks representing shear bands. Figure 22 shows SEM micrographs taken from the uniformly

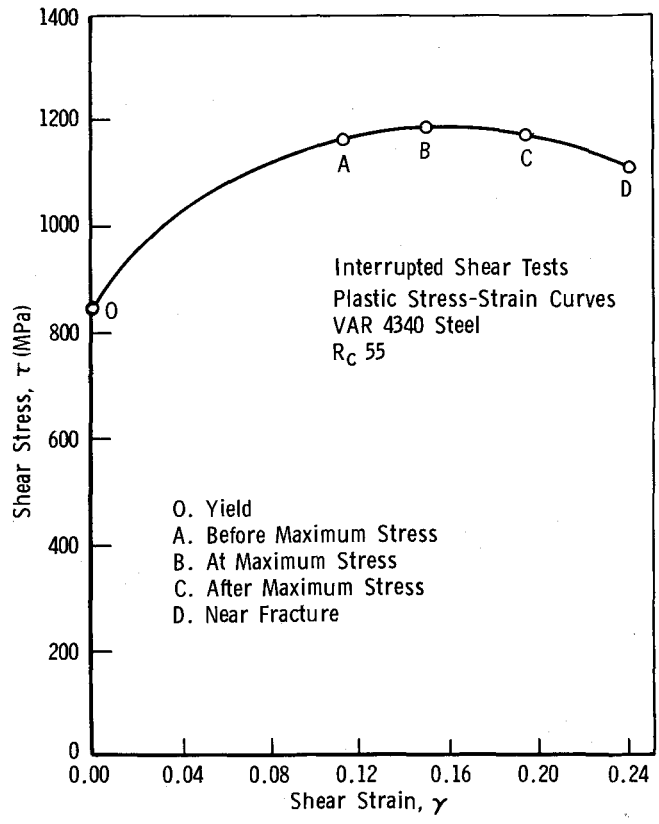

Fig. 20—Shear stress-strain curve of a VAR 4340 steel at Rc 55. Interrupted tests were performed to the points indicated (A to D).

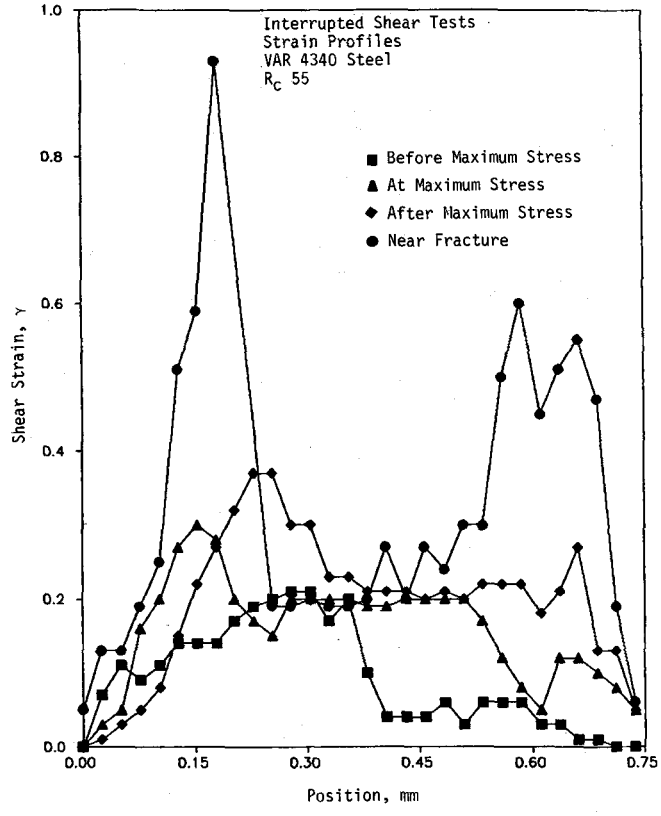

Fig. 21—Strain profiles obtained from the interrupted shear tests of a VAR 4340 steel at Rc 55. Interrupted tests were performed to the points indicated (A to D) in Fig. 20.

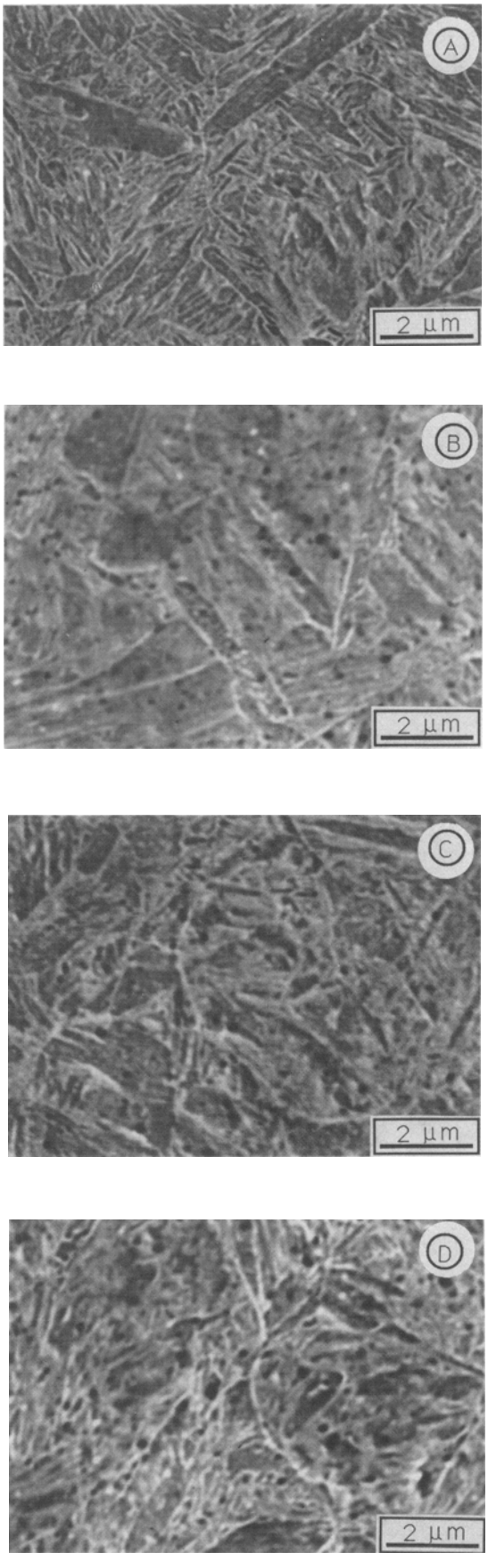

Fig. 22—Photomicrographs of the interrupted shear test specimens of a VAR 4340 steel at Rc 55: (*a*) before maximum stress; (*b*) at maximum stress; (*c*) after maximum stress; (*d*) near fracture.

deformed portions of the four specimen gage sections. Microvoids commensurate with the carbide particle size appear abruptly at the instability strain (B) with little change in microvoid density within the uniformly strained region as localized deformation proceeds elsewhere. Techniques for enhancing the contrast between microvoids and particles are under investigation. The abrupt appearance of microvoids supports a nucleation-controlled rather than growth-controlled softening mechanism.

Initially, the authors believed that the voids observed in both the thin foil specimens and polished and etched specimens were the result of preferential etching. However, these voids were not observed in the unstrained specimens. Additionally, microvoid sheets with void diameters roughly equivalent to the interparticle spacing were observed on the fracture surfaces of the shear specimens tested to fracture (Figure 23).

V. SUMMARY

The combined experimental evidence strongly suggests that strain localization in these UHS steels under pure shear loading conditions is driven by microvoid softening controlled by nucleation at 100 nm scale second-phase particles. These tests emphasize a void nucleation rather than void growth as the destabilizing event. This is supported by an observed pressure dependence of the instability strain, enhanced resistance to shear instability with particle dissolution, and direct observation of microvoids at these particles in deformed material. These experimental results coupled with analytical analyses,[16,17,18] indicate that microvoid nucleation and, hence, shear instability are dependent on the interparticle distance-to-particle radius ratio. In 4340 and 4130 steels, superior shear instability resistance for a given hardness is obtained in Stage I tempered microstructure where the only microvoid-nucleating particles appear to be those undissolved during austenitizing. Fine dispersoids play

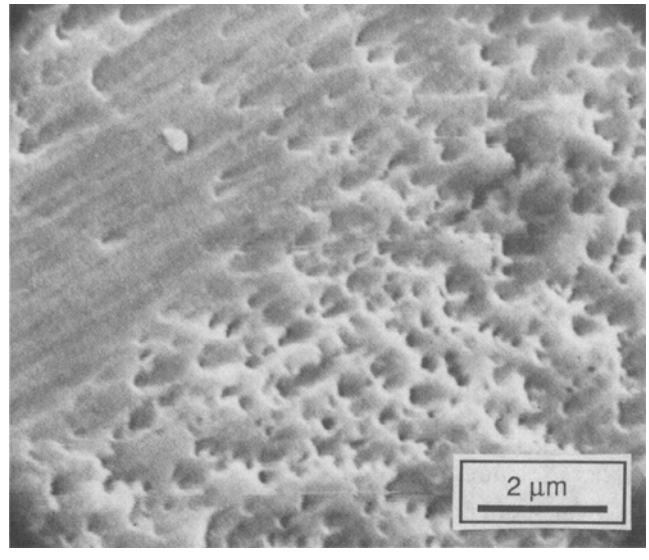

Fig. 23—Fractograph of a torsional shear specimen (AM 4340 steel at Rc 56) tested to failure, illustrates microvoid sheet type fracture mechanism.

a greater role than the larger inclusions in void formation in shear. The secondary hardening AF 1410 shows a much higher resistance to shear localization when cementite particles are fully dissolved by alloy carbide precipitation. For these steels at hardness near Rc 50, a direct correlation between G_{Ic} fracture toughness and shear instability strain is demonstrated. Continued study of microvoid nucleation in pure shear experiments will allow quantification of the role of a critical component of microstructure. Deliberate control of microvoid nucleating particle dispersion offers the potential for design of materials with greatly enhanced resistance to shear localization and ductile fracture.

REFERENCES

1. M. Azrin, J. Cowie, and G. Olson: *Annals of Israel Physical Society*, 1986, vol. 8, pp. 409-17; also Report No. MTL TR 87-2, U.S. Army Materials Technology Laboratory, Watertown, MA, Jan. 1987.
2. J. Mescall and R. Papirno: *Exp. Mech.*, 1979, vol. 9, pp. 283-311.
3. J. Cowie and F. Tuler: *Mat. Sci. and Eng.*, 1987, vol. 95, pp. 93-99.
4. H. Rogers: ARO Technical Report, U.S. Army Research Office, Durham, NC, May 1974.
5. H. Rogers: *Ann. Rev. Mater. Sci.*, 1979, vol. 9, pp. 283-311.
6. A. Bedford, A. Wingrove, and K. Thompson: *J. Aust. Inst. Metals*, 1974, vol. 9, pp. 61-74.
7. R. Clifton: Report No. NMAB-356, National Materials Advisory Board Committee, Washington, DC, 1980, ch. 8.
8. A. Argon: *The Inhomogeneity of Plastic Deformation*, 1st Ed., ASM, Metals Park, OH, 1973, pp. 161-89.
9. L. Samuels and I. Lamborn: in *Metallography in Failure Analysis*, 1st ed., Plenum Press, New York, NY, 1978, pp. 167-90.
10. G. Olson, J. Mescall, and M. Azrin: in *Shock Waves and High-Strain-Rate Phenomena in Metals*, Plenum Press, New York, NY, 1981, ch. 14.
11. T. Walker and M. Shaw: in *Advances in Machine Tool Design and Research*, Pergamon Press, New York, NY, 1969, p. 241.
12. H. Luong: Monash University, Victoria, Australia, unpublished Ph.D. thesis, 1977.
13. H. Luong: *Proceedings of the Australian Conference on Manufacturing Engineering*, Monash University, Victoria, Australia, 1977, p. 122.
14. D. Tracey and P. Perrone: U.S. Army Materials Technology Laboratory, Watertown, MA, unpublished research, 1986.
15. M. Gore, G. Olson, and M. Cohen: *Proceedings of the 34th Sagamore Army Materials Research Conference*, in press.
16. D. Tracey and P. Perrone: *Proceedings of the 34th Sagamore Army Materials Research Conference*, in press.
17. A.S. Argon, J. Im, and R. Safoglu: *Metall. Trans. A*, 1975, vol. 6A, pp. 825-37.
18. A.S. Argon and J. Im: *Metall. Trans. A*, 1975, vol. 6A, pp. 839-51.
19. J. Hutchinson and V. Tvergaard: *Proceedings of the 34th Sagamore Army Materials Research Conference*, in press.
20. M. Schmidt and R. Hemphill: *Proceedings of the 34th Sagamore Army Materials Research Conference*, in press.